Design of lateral and vertical $Bi_4O_5I_2$/BiOCl heterojunctions with different charge migration pathway for efficient photoredox activity[☆]

Yi Zhong [a], Chenglin Wu [a], Daimei Chen [a,*], Jinzhong Zhang [c], Yanmei Feng [a], Kang Xu [d], Weichang Hao [d,*], Hao Ding [a,*], Guocheng Lv [a], Yi Du [e], Lianzhou Wang [b,*]

[a] Engineering Research Center of Ministry of Education for Geological Carbon Storage and Low Carbon Utilization of Resources, Beijing Key Laboratory of Materials Utilization of Nonmetallic Minerals and Solid Wastes, National Laboratory of Mineral Materials, School of Material Sciences and Technology, China University of Geosciences, Beijing 100083, China
[b] Nanomaterials Centre, School of Chemical Engineering and Australian Institute for Bioengineering and Nanotechnology (AIBN), the University of Queensland, St Lucia, QLD 4072, Australia
[c] Department of Chemistry and Biochemistry, University of California, Santa Cruz, CA 95064, USA
[d] School of Physics and Centre of Quantum and Matter Sciences, International Research Institute for Multidisciplinary Science, Beihang University, Beijing 100191, China
[e] Institute for Superconducting and Electronic Materials (ISEM) Australian Institute for Innovative Materials (AIIM) University of Wollongong, New South Wales 2500, Australia

ARTICLE INFO

ABSTRACT

As 2D heterojunction photocatalysts, lateral heterojunctions (LHs) formed based on chemical bonding generally exhibit much higher photocarrier separation efficiency than vertical heterojunctions (VHs) formed by van der Waals bonds. However, little is known about the different detailed interfacial structures and photocarrier separation mechanisms of the two heterojunctions. Herein, 2D BiOCl and $Bi_4O_5I_2$ were selected as model building blocks to construct BiOCl/$Bi_4O_5I_2$ VHs and LHs. The LHs with direct charge carrier transport channels show stronger interfacial electric field and higher charge transfer efficiency than the VHs. The photogenerated charge carrier migration pathway in the LHs follows a Z-scheme model, while the VHs fits a type II model. As a result, the BiOCl/$Bi_4O_5I_2$ LHs exhibited higher redox performance than the VHs, which is 1.55, 1.56 and 2.1 times better for H_2 production, Cr(VI) photoreduction and phenol photodegradation, respectively. This study demonstrates a new approach to constructing highly efficient facet-dependent 2D heterojunction photocatalysts.

1. Introduction

Semiconductor photocatalysis has been considered as an efficacious and sustainable technique for addressing environmental pollution and energy issues because it can utilize solar-light to generate chemical energy [1–3]. To date, many photocatalysts such as TiO_2, g-C_3N_4, bismuth-based oxides and sulfides have been extensively studied for pollutant degradation, photocatalytic water splitting and CO_2 reduction [4–7]. However, practice applications of photocatalysis are greatly hindered by ineffective utilization of solar-light and low quantum efficiency due to the significant recombination of photoinduced electron–hole pairs. Heterojunctions based on two materials with complementary properties can harvest broad solar light and improve photoexcited charge separation due to the internal electric field formed at the interface. Therefore, construction of suitable heterojunctions is of strong interest for photocatalysis.

Recently, two-dimensional (2D) semiconductors with unique ultrathin layered structures have demonstrated distinct advantages as photocatalysts [8–10]. Due to their layered nature, 2D materials offer a platform to create heterojunctions with a variety of properties. These atomic monolayers can serve as building blocks and can be flexibly stacked vertically to create vertical heterojunctions (VHs) or stitched together seamlessly in-plane to form lateral heterojunctions (LHs) [11, 12]. The VHs with the monolayers between different materials coupled together though the van der Waals (VDW) force can be relatively straightforwardly fabricated and have demonstrated excellent photocatalytic activity due to atomically sharp interface and tunable band alignment [13]. On the other hand, LHs [14] based on chemical bonding

of different materials are more challenging to construct and have only been limited to a few systems such as transition-metal dichalcogenides (MoS$_2$/MoSe$_2$ [15], MoS$_2$/WS$_2$ [16]), because strict restrictions in lattice match of various components. Interfacial electric field (IEF) is a key factor for charge separation/transportation [17–19]. Generally, IEF induced by chemical bonding is much stronger than that from VDW force. Thus, construction of LHs is of strong interest in the development of photocatalysis. Furthermore, the behavior of photogenerated charges at the interface may differ substantially between VHs and LHs, but this has not been studied.

In general, based on the photocarrier transfer pathway, heterojunctions can be divided into type II and Z-scheme. In type II systems, the photogenerated electrons and holes are effectively separated due to the good match of bandgap energy levels between these two semiconductors. However, the redox ability of the photogenerated electrons and holes are often weakened in the type II heterojunctions as the photogenerated electrons in the conduction band (CB) of one semiconductor would transfer into the CB of another semiconductor with relatively lower CB band edge position, while the hole in the valence band (VB) of the second semiconductor would transfer to the valence band (VB) of the first semiconductor with the higher VB position. Different from the type II system, the Z-scheme heterojunctions not only allow for photogenerated electrons and holes space separation, but also retain the strong reduction and oxidation ability [50]. The photogenerated electrons of one semiconductor would be recombined with holes of another semiconductor, leaving the more electrons and holes with higher redox ability take part into the photocatalytic reduction and oxidation reaction [51,52]. Therefore, designing and constructing Z-scheme heterojunctions are attractive for higher performance photocatalyst but still challenging to achieve in practice.

BiOCl has 2D [Cl−Bi−O−Bi−Cl] layered structure due to VDW interaction [20]. It favors a formation of thin-layer structure with exposure of (001) top facets and (110) lateral facets, providing a great chance to construct vertical and lateral heterojunctions [21]. Bi$_4$O$_5$I$_2$ is another kind of 2D photocatalyst with narrow band gap of 2.1 eV. It is generally used as a visible-light sensitizer to extend light absorption [22]. Considering the layered structure and the small lattice mismatch between Bi$_4$O$_5$I$_2$ (303) slab (5.8 Å) and BiOCl (110) slab (5.52 Å), Bi$_4$O$_5$I$_2$ may selectively grow along (001) and (110) facets of BiOCl to form VHs and LHs.

In this work, BiOCl and Bi$_4$O$_5$I$_2$ were selected as model photocatalysts to fabricate VHs and LHs. The monoclinic phase Bi$_4$O$_5$I$_2$ nanosheets are naturally prone to grow on the BiOCl (001) facet via VDW interactions to form BiOCl/Bi$_4$O$_5$I$_2$ VHs (BOC-I-V) via a facile hydrothermal method. For comparison, we also deliberately designed a unique laterally grown BiOCl/Bi$_4$O$_5$I$_2$ LHs (BOC-I-L) by epitaxial growth of Bi$_4$O$_5$I$_2$ on the BiOCl (110) facet using a polyvinyl pyrrolidone (PVP) insulating layer to cover the BiOCl (001) top facet due to the well match of Bi$_4$O$_5$I$_2$ (303) slab with BiOCl (110) slab. The BOC-I-L exhibited the strongest photoreduction and photodegradation activity among the sample of pure BiOCl, pure Bi$_4$O$_5$I$_2$ and the BOC-I-V. This is attributed to its wider visible-light absorption, lager IEF, higher charge transfer/separation efficiency, and unique photogenerated charge carrier migration pathway. This work has important implications in environmental issues.

2. Experimental

2.1. Materials

The polyvinyl pyrrolidone (PVP, Mw = 80000), bismuth nitrate pentahydrate (Bi(NO$_3$)$_3$·5 H$_2$O, 99.99%), sodium chloride (NaCl, 99.5%), glycerol (99.9%), potassium iodide (KI, 99.5%), ethanol anhydrous (analytical grade) were purchased from the Aladdin Industrial Co., Ltd. All the chemical reagents were analytical grade and used without any further purification.

2.2. Synthesis of BiOCl nanosheets

4.00 mmol Bi(NO$_3$)$_3$·5 H$_2$O and 4.00 mmol KCl were dissolved in 80 ml deionized water under stirring continuously for one hour. Then, the mixed solution was transferred to a Teflon-lined stainless-steel autoclave and heated at 160 °C for 16 h (h). After cooling to room temperature, the product was collected, then washed several times with deionized water and ethanol, and dried at 60 °C for 12 h in a vacuum atmosphere.

2.3. Synthesis of Bi$_4$O$_5$I$_2$

4.00 mmol Bi(NO$_3$)$_3$·5 H$_2$O was dissolved in 40 ml glycerol under magnetic stirring for 1 h, meanwhile, 4.00 mmol KI dissolved in another 40 ml glycerol under magnetic stirring for one hour. Then, KI solution was added drop-wise into the above Bi(NO$_3$)$_3$·5 H$_2$O solution under continuously stirring for one hour. The uniform suspension solution was transferred into 100 ml Teflon-lined stainless-steel autoclaves and maintained at 180 °C for 16 h followed by naturally cooling to room temperature. The Bi$_4$O$_5$I$_2$ precursor powder was obtained by centrifugation and washed with distilled water and absolute ethanol for several times, then dried at 80 °C for 12 h under vacuum atmosphere.

0.3 g of Bi$_4$O$_5$I$_2$ precursor was dispersed in 100 ml deionized water at 50 °C under stirring. The Bi$_4$O$_5$I$_2$ product were gained by a facile hydrolytic process. Finally, washed with deionized water for several times and dried at 80 °C.

2.4. Preparation of BOC-I-V heterojunction

0.1 g BiOCl was dispersed in 100 ml deionized water through sonication, and then continued to be ultrasonicated for four hours to form a homogeneous mixed solution. Subsequently, M mg (M = 10.0, 30.0, 60.0) Bi$_4$O$_5$I$_2$ precursor powder was added into the above dispersion under stirring in a 50 °C water bath. After further stirred for one hour, the mixture solution was transferred to a Teflon-lined stainless-steel autoclave and heated at 100 °C for one hour. The resultant product was separated by centrifugation and washed with ethanol and water for several times. The final product was then dried at 60 °C for 12 h. According to the addition amount of M (M = 10.0 mg, 30.0 mg, 60.0 mg), the collected products are denoted as BOC-I-V1, BOC-I-V2, BOC-I-V3, respectively.

2.5. Preparation of BOC-I-L heterojunction

BOC-I-L Heterojunction was obtained with a similar preparation procedure of BOC-I-V Heterojunction except for the addition of PVP as insulating layer in the reaction solution. In detail, 0.1 g BiOCl and 0.2 g PVP was dispersed in 100 ml deionized water and ultrasonicated for four hours to form a homogeneous mixed solution. Subsequently, M mg (M = 10.0 mg, 30.0 mg, 60.0 mg) Bi$_4$O$_5$I$_2$ precursors powder was added into the dispersion under stirring in a 50 °C water bath. The mixture solution was further sonicated for one hour, then transferred to a Teflon-lined stainless-steel autoclave, and heated at 100 °C for one hour. After the autoclave had cooled down to room temperature, the resultant product was separated by centrifugation and washed with ethanol and water for several times to remove excess PVP. The final product was then dried at 60 °C for 12 h. According to the addition amount of M (M = 10.0 mg, 30.0 mg, 60.0 mg), the collected products are denoted as BOC-I-L1, BOC-I-L2, BOC-I-L3, respectively.

2.6. Characterization

The characterization details of the photocatalysts be provided in the Supporting Information (SI).

2.7. Performance of photocatalytic redox

2.7.1. Photocatalytic H₂ evolution

The experiment was carried out on a photoreactor (Pyrex glass) connected with a closed circulation system (Lab solar-III AG, Beijing Perfect light Technology Co., Ltd., China). In the experiment, a certain amount of photocatalyst (50 mg), 90 ml distilled water, Co-catalyst (0.3 wt% H_2PtCl_6) and 10 ml sacrificial agent (Lactic acid) were added in the quartz reactor. Then, high-purity Ar gas was bubbled through the solution for one hour to remove air from quartz reactor. Subsequently, they were irradiated by a 300 W Xe lamp with an AM 1.5 G filter (100 mW·cm^{-2} in intensity) with keeping the reactor temperature ~ 20 °C via a recirculating cooling water system. Then, 1.00 ml of the gaseous product was sampled and inspected using GC-2014 C gas chromatograph (Shimadzu Corporation of Japan).

2.7.2. Photocatalytic Cr (VI) reduction

The sample (30 mg) was added into a quartz tube (60 ml) containing 50 ml of pollutant aqueous solution containing 20 mg·L^{-1} of Cr (VI). Stirring magnetically for 1 h in the dark to achieve the dark adsorption-desorption equilibrium. Then, the photocatalytic system was exposed to light (λ = 300–780 nm). 5.00 ml of suspension is taken out in the same time interval. The Cr (VI) concentration in solution was measured using the 1,5-diphenylcarbazid analytical method with a UV–vis spectrophotometer uv-3900 ultraviolet spectrophotometry.

2.7.3. Photocatalytic phenol degradation

The photocatalytic oxidation performance of the sample is characterized by photocatalytic degradation of phenol. The sample (30 mg) was added into a quartz tube (60 ml) containing 50 ml of 10 mg·L^{-1} of phenol. Before the light irradiation (Phchem III 12-bit Photochemical Reactor, Beijing Newbit λ = 300–780 nm, light intensity =100 mW·cm^{-2}), the dispersion was stirred magnetically for one hour in the dark to achieve the dark adsorption-desorption equilibrium. 5.00 ml of suspension is taken out in the same time interval. The concentration of Phenol was measured by high-performance liquid chromatography (HPLC, U3000, Thermo Fisher Scientific) with a C18 column. The mobile phase contains 55% methanol and 45% water. The flow rate is 0.8 ml/min, and the detection wavelength is 270 nm.

3. Results and discussion

3.1. Structure and morphology of BOC-I-V and BOC-I-L heterojunction

Fig. S1a and S1b show the crystal structure of the tetragonal phase BiOCl and monoclinic phase $Bi_4O_5I_2$. The tetragonal phase BiOCl nanosheets with co-exposed (001) facet and (110) facets [56], prepared via one-step hydrothermal reaction, are in the size range of about 300 nm ~ 2 μm (Fig. 1a-c) and its thickness is about 32.3 nm (Fig. 1 g, h). Compared with BiOCl nanosheets, the size of $Bi_4O_5I_2$ is much smaller, which is in range of tens of nanometers and its thickness is only about 5 nm (Fig. 1d-f, i and j). Both BiOCl and $Bi_4O_5I_2$ have nanosheet structures. Fig. S2 summarizes the preparation scheme for BOC-I-V and BOC-I-L heterojunction. BiOCl/$Bi_4O_5I_2$ VHs would be constructed simply and controllable by two step hydrothermal method due to that there is no strict lattice match for fabricating VHs heterojunctions and the small 2D $Bi_4O_5I_2$ nanosheet are naturally prone to couple with big BiOCl nanosheet for decreasing surface energy [57]. The BiOCl/$Bi_4O_5I_2$ LHs would
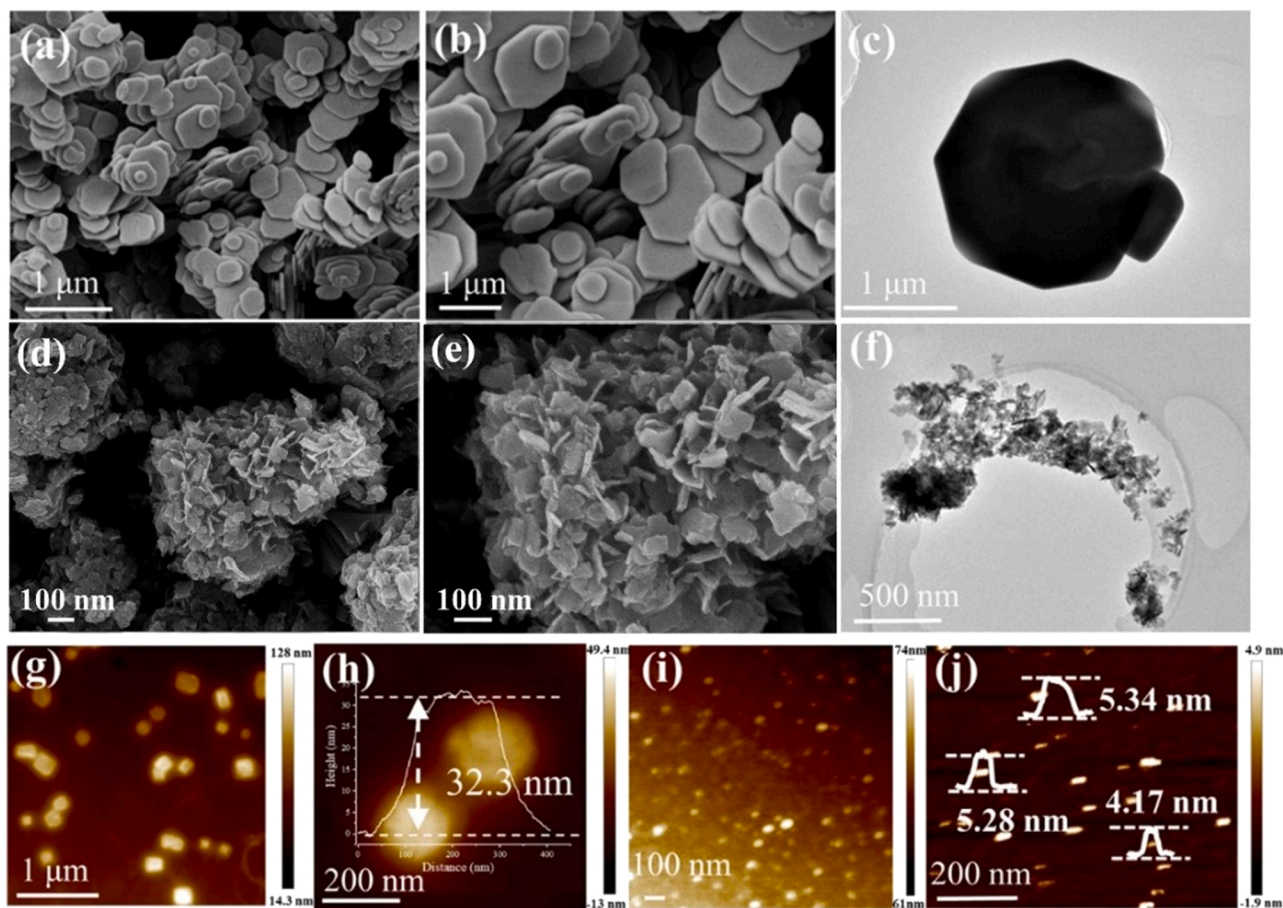

Fig. 1. (a, b) SEM image of BiOCl, (c) TEM image of BiOCl; (d, e) SEM image of $Bi_4O_5I_2$, (f) TEM image of $Bi_4O_5I_2$; (g, h) AFM image of BiOCl, the inset in the figure indicates the thickness of BiOCl; (i, j) AFM image of $Bi_4O_5I_2$, the inset in the figure represents the thickness of $Bi_4O_5I_2$.

be prepared by selectively growth of $Bi_4O_5I_2$ on the BiOCl (110) facet with a polyvinyl pyrrolidone (PVP) as the insulating layer covering on the BiOCl (001) top facet [58].

Fig. 2a-e shows that the SEM and TEM images of BOC-I-V heterojunctions. The SEM images show that small $Bi_4O_5I_2$ nanosheets are flexibly stacked vertically on top of the BiOCl (001) facet (Fig. 2a-b, S3), which increase with $Bi_4O_5I_2$ precursor concentration (Fig. S3), suggesting that the $Bi_4O_5I_2$ growth is favored on the BiOCl (001) facet [57]. The TEM images of BOC-I-V heterojunctions (Fig. 2c, d) also show a hybrid structure with small sheets stacked on the surface of the BiOCl (001) facet, supporting the formation of BOC-I-V heterojunctions. The high-resolution transmission electron microscopy (HR-TEM) image (Fig. 2e) of the BOC-I-V heterojunctions confirms that the small sheets are $Bi_4O_5I_2$ with lattice fringes of 0.274 nm, corresponding to the $Bi_4O_5I_2$ (303) facet [25], while the large sheet is BiOCl with lattice fringes of 0.275 nm corresponding to the (110) facet [26]. The fast Fourier transform (FFT) images taken from the TEM of BiOCl and $Bi_4O_5I_2$ are consistent with the lattice fringes of them (Fig. 2e). The FFT

images of BOC-I-V heterojunction interface shows that the BiOCl and $Bi_4O_5I_2$ are different in their orientation (Fig. 2f-h), suggesting a likely relaxation of the lattice match requirements for VHs [27]. The energy dispersive x-ray spectroscopy (EDS) results in Fig. S4 and S5 show that Bi, O, Cl, I elements are uniformly dispersed on the surface of BiOCl (001) facet and the I elements are hardly observed on the surface of BiOCl (110) facet, further supporting the formation of BOC-I-V heterojunction. A schematic diagram for the BOC-I-V heterojunctions and their corresponding crystal structures is shown in Fig. 2i-l. The interaction between layers in 2D layered materials involves VDW force [45–47]. Both BiOCl and $Bi_4O_5I_2$ are typical 2D layered structures and the BOC-I-V heterojunction is formed most likely due to VDW force between the two materials.

Fig. 3 shows SEM and TEM images of BOC-I-L heterojunctions. The SEM images (Fig. 3a, b, S6) show that the (001) top facet is smooth, and much small nanosheets were grown on the (110) facet of BiOCl. The TEM images show a clear brightness-difference between the middle and edge part of as-prepared sample (Fig. 3c, d), which further demonstrated
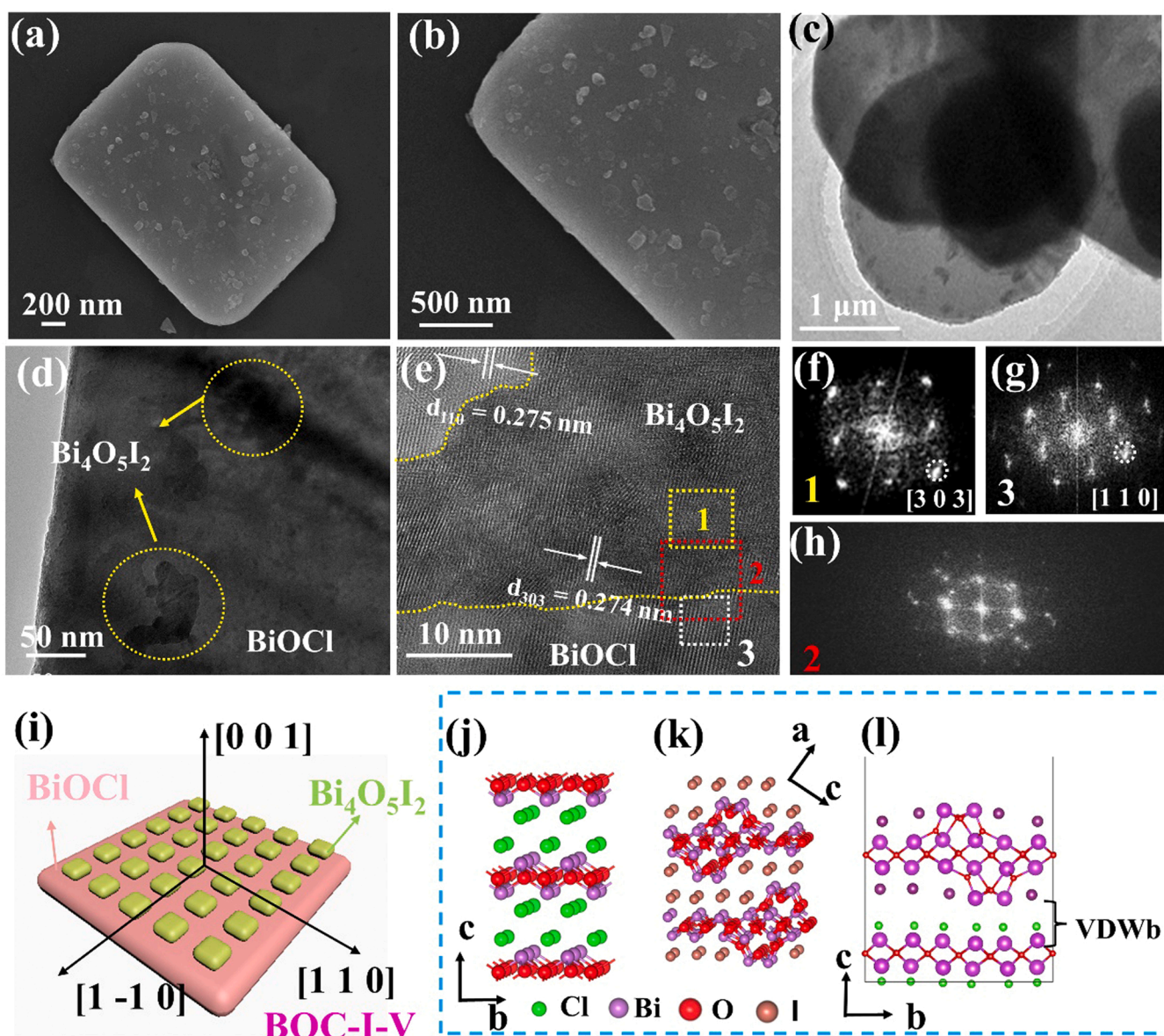

Fig. 2. (a, b) SEM images of BOC-I-V heterojunction, (c, d) TEM and HR-TEM (e) image of BOC-I-V heterojunction, (f-h) schematic diagram of the diffraction spot corresponding to the box in Fig. e, yellow (f): $Bi_4O_5I_2$, red (h): interface, white (g): BiOCl, (i) model schematic diagram of BOC-I-V heterojunction, (j-l) schematic diagram of the crystal structure of BiOCl, $Bi_4O_5I_2$, BOC-I-V heterojunction.
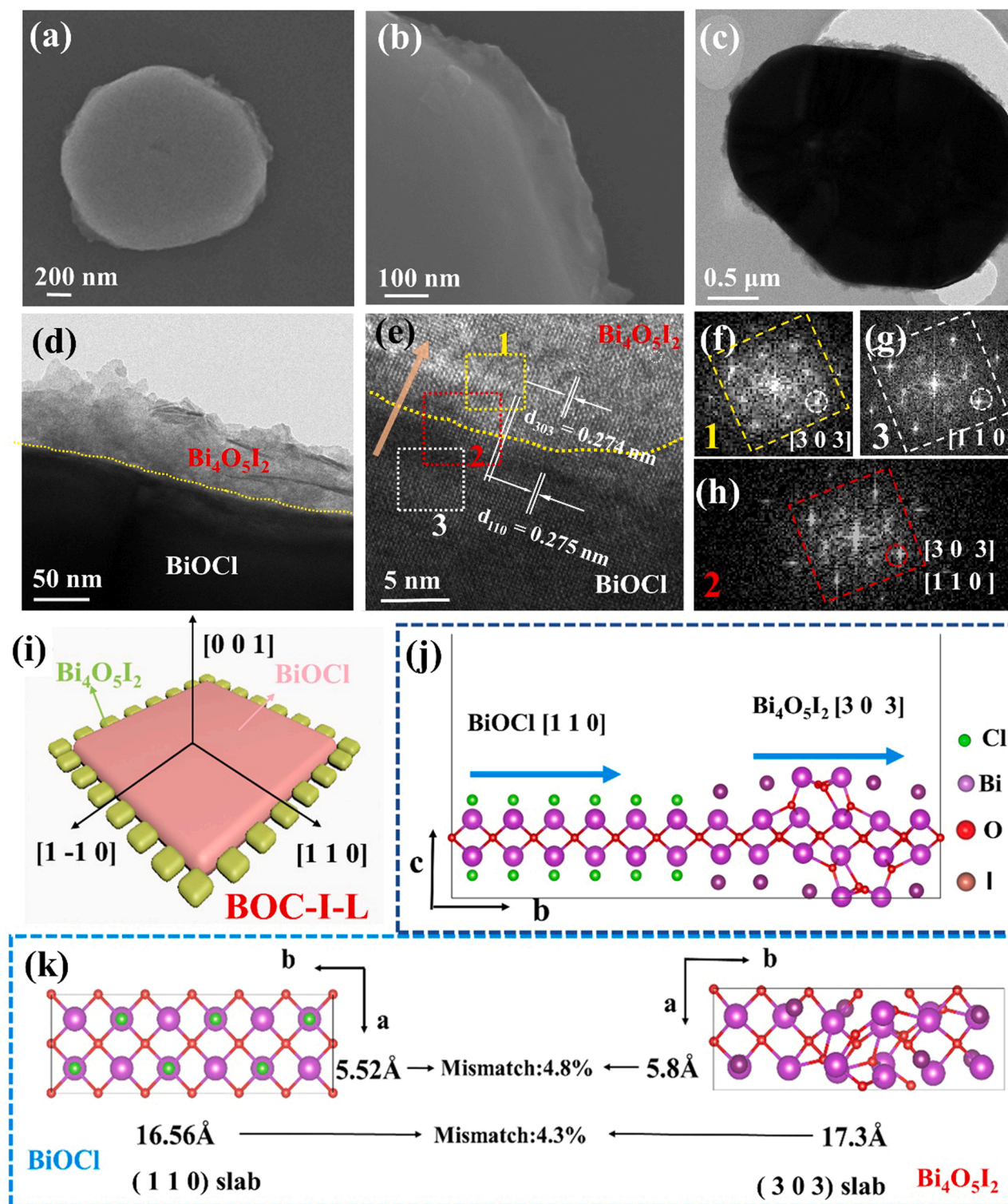
Fig. 3. (a, b) SEM image of BOC-I-L heterojunction, (c, d) TEM image of BOC-I-L heterojunction, (e) the HR-TEM image of BOC-I-L heterojunction, (f-h) schematic diagram of diffraction spots corresponding to the box in panel e, yellow (f): $Bi_4O_5I_2$, red (h): interface, white (g): BiOCl, (i) schematic model of BOC-I-L heterojunction, (j) schematic diagram of the crystal structure of the BOC-I-L heterojunction, (k) lattice mismatch of BiOCl (110) slab and $Bi_4O_5I_2$ (303) slab.

that the $Bi_4O_5I_2$ nanosheets stand on the (110) facet of BiOCl. From the HR-TEM image of the interface of heterojunction, the lattice fringes of 0.275 nm correspond to the BiOCl (110) side facet (Fig. 3e) [26] and the lattice fringes of 0.274 nm match well with the $Bi_4O_5I_2$ (303) facet [25], the continuous lattice fringes from dark to bright areas (Fig. 3e) suggest that the perfect lateral epitaxial heterojunction with a tight

heterojunction-interface. FFT images taken from TEM of BiOCl and $Bi_4O_5I_2$ are consistent with lattice fringes of them. In addition, the FFT analysis of BOC-I-L heterojunction interface displays quite similar structure with the same orientation along the BiOCl (110) and $Bi_4O_5I_2$ (303) facet (Fig. 3f-h), further confirming the epitaxial growth of $Bi_4O_5I_2$ nanosheets along BiOCl (110) facet [23,24]. The EDS mapping of

BOC-I-L profile (Fig. S7 and S8) shows that the O, I, Bi, Cl elements are uniform distributed on the BiOCl (110) facet and the I element could rarely be observed on the surface BiOCl (001) facet. Meanwhile, element line of Cl and I atoms were carried out on the edge part of sample (Fig. S7b), the Cl element has a larger presence in the middle part than on the edges, while the I element has a smaller presence in the middle part than on the edges, which strongly supports of the formation BOC-I-L heterojunctions. A schematic for the BOC-I-L and its corresponding crystal structure is given in Figs. 3i and 3j. $Bi_4O_5I_2$ nanosheets epitaxially grow along the BiOCl (110), and would be connected with BiOCl by chemical band of Bi-O-Bi (Fig. 3j). The lattice structures of BiOCl (110) and $Bi_4O_5I_2$ (303) are given in Fig. 3k to illustrate the possible epitaxial growth of $Bi_4O_5I_2$ along BiOCl (110). The crystal lattice constant of BiOCl (110) slab is 5.52 Å, and that of $Bi_4O_5I_2$ (303) slab is 5.80 Å. The small lattice mismatch of 4.8% and crystal symmetry between BiOCl (110) slab and $Bi_4O_5I_2$ (303) slab provide the likely condition for the epitaxially growth of $Bi_4O_5I_2$ nanosheets along the BiOCl (110) facet, resulting in the formation of BOC-I-L heterojunctions.

The XRD patterns shown in Fig. S10a show that the BiOCl is in the tetragonal phase, based on the standard card (JCPDS No. 6–249). The diffraction peaks of $Bi_4O_5I_2$ at 29.6°, 31.6°, 45.4°, 54.3° correspond to (−4 to 11), (402), (422), (811) crystal facet of monoclinic phase, respectively [28]. The XRD diffraction peaks of BOC-I-V and BOC-I-L heterojunctions can be indexed to BiOCl and $Bi_4O_5I_2$ without any impurity peaks (Fig. S10a). Fig. S10b shows that the (001)/(110) peak intensity ratio in the BiOCl sample is 2.43, while that decreases to 1.52 in BOC-I-V and increase to 5.07 in the BOC-I-L, suggesting that the selective growth of $Bi_4O_5I_2$ affects the intensity ratio of BiOCl facet [28–31]. With the increase in the loading amount of $Bi_4O_5I_2$ loading from 10 mg to 60 mg, the intensity ratio of BiOCl (001)/(110) facet decreases from 1.87 to 1.11 in the BOC-I-V heterojunction, while gradually increases from 3.37 to 6.57 in the BOC-I-L heterojunction (Fig. S10c, d), suggesting that the intensity of BiOCl different facet is related to the growth orientation and loading amount of $Bi_4O_5I_2$ on the BiOCl surface. This phenomenon further supports that most of $Bi_4O_5I_2$ grow on the BiOCl (001) facet in the BOC-I-V heterojunctions, while $Bi_4O_5I_2$ nanosheets grow on the BiOCl (110) facet in BOC-I-L [17,29].

3.2. Charge transfer mechanism of BOC-I-V and BOC-I-L heterojunction

To gain an insight into the separation and transfer mechanisms of photogenerated carriers in the BOC-I-V and BOC-I-L heterojunctions, in situ Kelvin probe force microscopy (KPFM) with 360 nm laser (Fig. S11) was used to study the surface potential at the heterojunction interface [43,48]. Fig. 4a, b shows the SEM and KPFM topography of the stacked nanosheet structure of the BOC-I-V heterojunctions. Similar to the SEM and TEM above, the small irregular $Bi_4O_5I_2$ nanosheets lay on the (001) surface of BiOCl. Figs. 4c and 4d show the surface potential maps of BOC-I-V heterojunctions in dark and under the irradiation of 360 nm laser, respectively, and their corresponding line profiles are compared in Fig. 4e. The local surface potential difference between $Bi_4O_5I_2$ (point B) and BiOCl (point A) is 13.4 mV under the dark (Fig. 4e). Under the light irradiation (Fig. 4d), the surface potential of $Bi_4O_5I_2$ increases from 7.5 mV to 17.0 mV, and the potential difference between them greatly increase to 33.1 mV (Fig. 4e), indicating the accumulation of photogenerated holes on the surface of $Bi_4O_5I_2$ and the accumulation of photogenerated electrons on the surface of BiOCl (001) [59]. Fig. S12 shows that the edge potential of BiOCl increase after the light irradiation, showing that photogenerated electrons form BiOCl (110) transfer to BiOCl (001). The KPFM results for the BOC-I-V heterojunctions suggest that the photogenerated electrons from the $Bi_4O_5I_2$ (30−3) facet migrate to the BiOCl (001) facet through the heterojunction interface (001)//(30−3), and the photogenerated holes are transferred from the BiOCl (001) facet to the $Bi_4O_5I_2$ (30−3) facet [60].

The charge transfer in BOC-I-V heterojunctions is further confirmed by the in situ irradiated X-ray photoelectron (ISI-XPS). The XPS survey

Fig. 4. BOC-I-V: (a) SEM morphology, (b) KPFM morphology, surface potential map under dark conditions (c) and 360 nm laser irradiation (d), (e) surface potential curve. (f-i) High-resolution XPS for (f) Cl 2p, (g) I 3d, (h) O1s and (i) Bi 4 f of BOC-I-V heterojunction in the dark or under 365 nm light irradiation. (j) SEM image of MnOx nanosheet-deposited BOC-I-V heterojunction and k) the corresponding schematic diagram; (l) SEM image of Pt nanoparticle-deposited BOC-I-V heterojunction and (m) the corresponding schematic diagram.

spectrum (Fig. S13) shows that the samples contain Bi, O, Cl, and I elements without noticeable impurities. The Cl 2p and I 3d spectra of the BOC-I-V heterojunctions show essentially no change in the dark (Fig. 4 f, g), suggesting little carrier diffusion at the heterojunction interface [32–34]. Whereas a negative peak shift in Cl 2p (0.2 eV) and a positive peak shift in I 3d (0.2 eV) were observed under 365 nm irradiation (Fig. 4f, g), further supporting that the transfer of photogenerated electron from $Bi_4O_5I_2$ to BiOCl. The shifts of O 1 s and Bi 4 f were also observed under light irradiation (Fig. 4h, i). In addition, two typical photo-deposition reactions were carried out to confirm the transfer mechanism of photogenerated electrons and holes using the H_2PtCl_6 and $MnCl_2$ as capture agents [35]. As expected, the MnOx nanosheets are mainly deposited on the BiOCl (110) facet (Fig. 4j, k), while the Pt nanoparticles are deposited on the BiOCl (001) facet (Fig. 4l, m). All results, including the XPS data, the KPFM and photo-deposition reactions, strongly support that photogenerated electrons transferred from the $Bi_4O_5I_2$ (30−3) facet to the BiOCl (001) facet, while the photogenerated holes transferred from the BiOCl (001) facet to $Bi_4O_5I_2$ (30−3) facet [35,36].

Fig. 5a and Fig. 5b show the SEM and KPFM topography of BOC-I-L with smooth surface. The epitaxial morphology demonstrates a well-defined BOC-I-L heterojunction, confirming the close contact between BiOCl and $Bi_4O_5I_2$. Fig. 5c and Fig. 5d give the surface potential map of BOC-I-L under dark and 360 nm laser irradiation, respectively, and their corresponding line profiles are compared in Fig. 5e. The BOC-I-L heterojunction displays uniform surface potential (259.5 mV) under the dark, which may be attributed to the formation of close contact epitaxial heterojunction via Bi-O-Bi carrier channel to balance the two-phase potentials [37]. This result is further confirmed by an obvious the negative shift of 0.3 eV in Cl 2p peak and the positive shift of 0.3 eV in I 3d peak in the XPS under the dark (Fig. 5f, g). The spontaneous charge diffusion at the interface of BOC-I-L without light irradiation results

from the Fermi level difference between BiOCl (001) facet and $Bi_4O_5I_2$ (30−3) facet.

Under light irradiation, the edge surface potential of BOC-I-L heterojunction is significantly reduced by 21.7 mV (Fig. 5e) and the interface between BiOCl and $Bi_4O_5I_2$ can be clearly observed (Fig. 5d), suggesting that the photogenerated electrons are mainly accumulated at the $Bi_4O_5I_2$ (30−3) facet and the photogenerated holes are accumulated in BiOCl (001) facet (Fig. S14). The large potential difference may be attributed to the established IEF and extremely facile transport of the photogenerated electrons and holes via direct carrier channel (Bi-O-Bi) at the interface of the BOC-I-L heterojunction [38]. Subsequently, the ISI-XPS results show a positive shift in the binding energies of Cl 2p (0.2 eV) and O 1 s (0.2 eV), and a negative shift in the binding energies of I 3d (0.2 eV) and Bi 4 f (0.1 eV) under the 365 nm light irradiation, suggesting that photogenerated electrons BiOCl (001) facet are transferred to $Bi_4O_5I_2$ (30−3) facet (Fig. 5f, g). The shifts of O 1 s and Bi 4 f were also observed under light irradiation (Fig. 5h, i). Besides, MnOx nanosheets are assembled on the (001) facet of BiOCl (Fig. 5j, k), and Pt nanoparticles are reduced and deposited on the $Bi_4O_5I_2$ (30−3) facet under the UV–vis light irradiation (Fig. 5 l, m) [35]. The above analysis strongly supports that photogenerated electrons from BiOCl (001) facet are transferred to $Bi_4O_5I_2$ (30−3) facet and combined with photogenerated holes of $Bi_4O_5I_2$ at the interface.

To reveal the band energy structure of BOC-I-V and BOC-I-L heterojunctions, the work function (WF) (Fig. 6a and b) and the density of states (DOS) (Fig. S15, S16) of BiOCl and $Bi_4O_5I_2$ are calculated by Density functional theory (DFT) calculation. The WF is calculated from the energy difference between the vacuum level and the Fermi energy level (E_F) based on the electrostatic potential of BiOCl and $Bi_4O_5I_2$, and closely related to the interfacial charge-transfer process. As shown in Fig. 6a, b, the BiOCl (001) facet (6.68 eV) have a higher WF than that of $Bi_4O_5I_2$ (30−3) facet (4.48 eV). The Kelvin probe test (Fig. S17) was
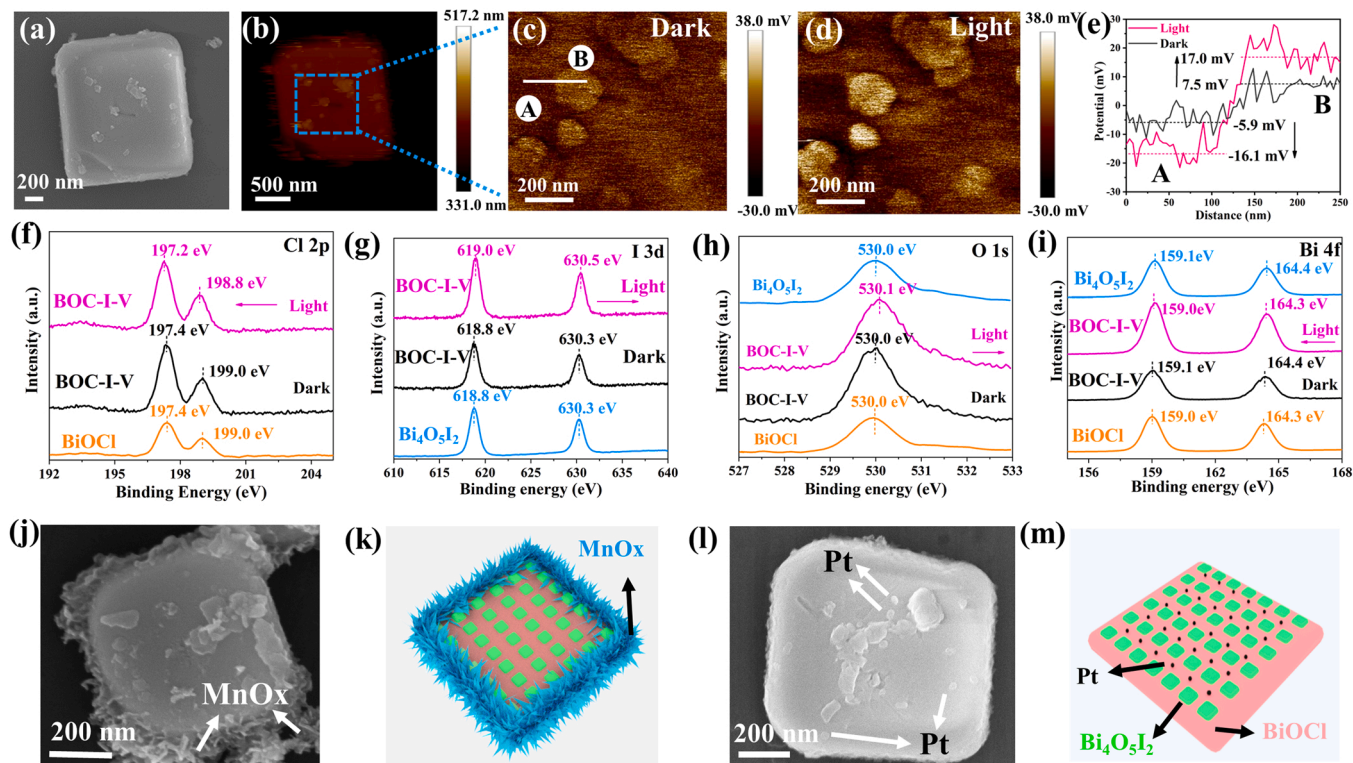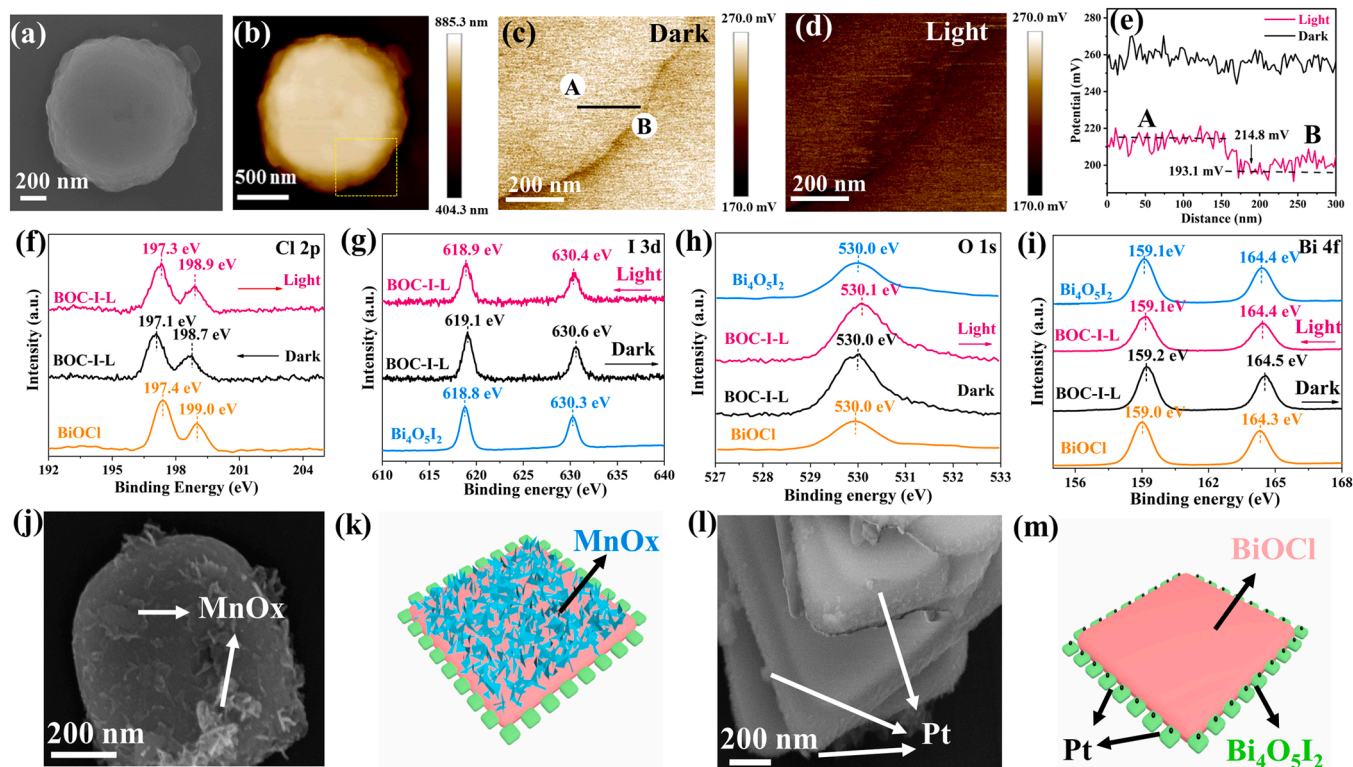

Fig. 5. BOC-I-L: (a) SEM morphology, (b) KPFM morphology, surface potential map under dark conditions (c) and 360 nm laser irradiation (d), (e) surface potential curve. (f-i) High-resolution XPS for (f) Cl 2p, (g) I 3d, (h) O1s and (i) Bi 4 f of BOC-I-L heterojunction in the dark or under 365 nm light irradiation. (j) SEM image of MnOx nanosheet-deposited BOC-I-L heterojunction and k) the corresponding schematic diagram; (l) SEM image of Pt nanoparticle-deposited BOC-I-L heterojunction and (m) the corresponding schematic diagram.

Fig. 6. Calculated electrostatic potentials for (a) BiOCl (001) facet and (b) Bi$_4$O$_5$I$_2$ (30−3) facet. The green, red, white and brown correspond to Cl, O, Bi, and I atoms, respectively, (c) lateral view and top view of charge density difference of BOC-I-L. The yellow and cyan-blue stan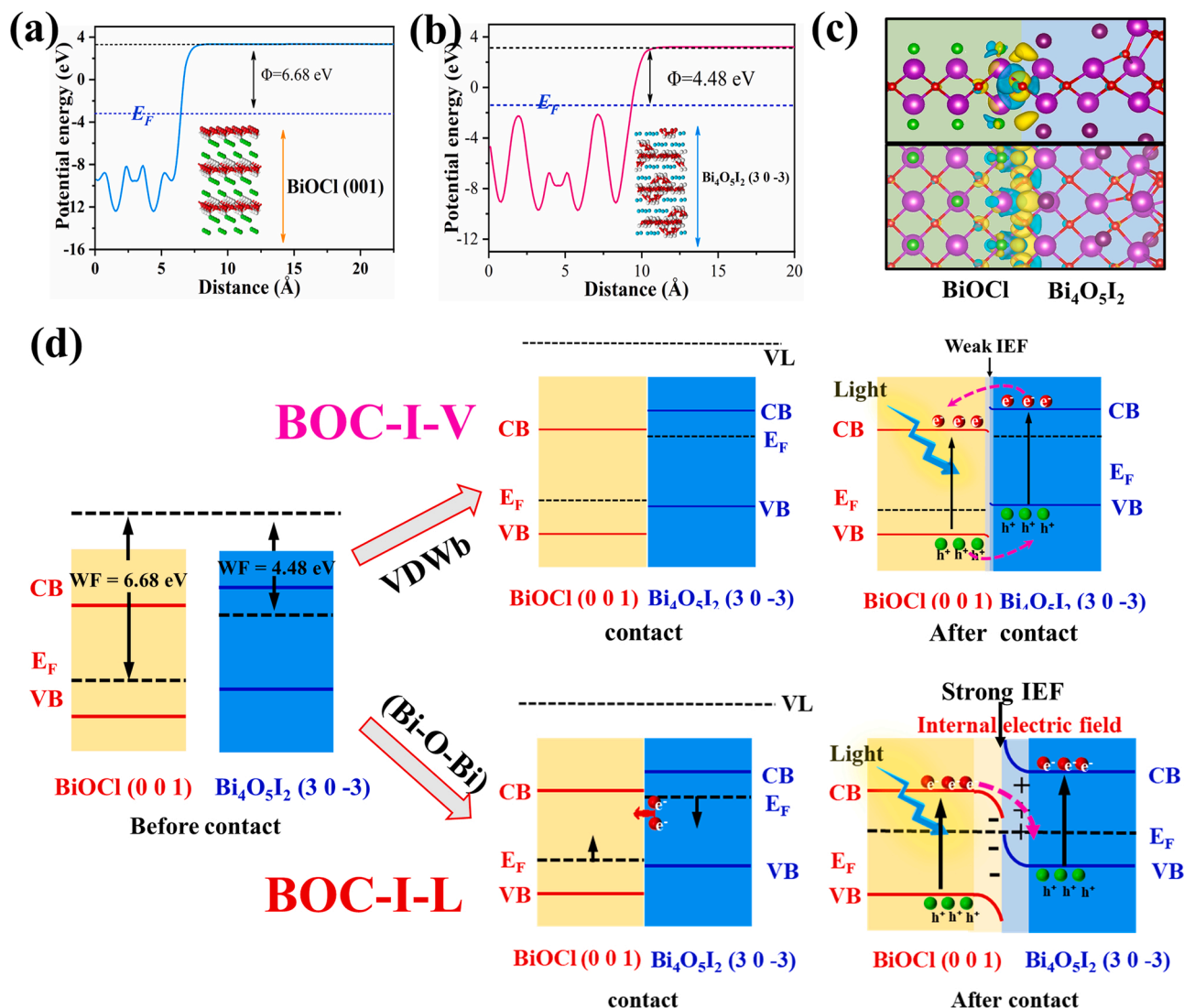d for the electron accumulation and depletion, respectively, (d) schematic diagram for the formation of IEF and the transport of photogenerated electrons between BiOCl (001) facet and Bi$_4$O$_5$I$_2$ (30−3) facet for BOC-I-V and BOC-I-L heterojunction.

used to further confirm the WF of BiOCl(001) (5.72 eV) and Bi$_4$O$_5$I$_2$(30−3) (5.22 eV), which is consistent with DFT calculation. When BiOCl and Bi$_4$O$_5$I$_2$ layers are in intimate contact in vertical direction (BOC-I-V heterojunction), although the Fermi energy levels are different, it is difficult to transfer electrons at the contact interface due to the BOC-I-V is weakly coupled via the VDW interaction without any chemical (covalent or ionic) bonding across the interface, and their interface layers possesses a chemically passivated surface, which is not beneficial to the spontaneous transfer of carriers at the interface [49]. Consequently, the band bending at the interface is too weak to form a strong IEF for driving the photogenerated charge migration [32,34]. With the match of the CB edges of BiOCl and Bi$_4$O$_5$I$_2$, the photogenerated electrons from the CB of Bi$_4$O$_5$I$_2$ tend to migrate to the CB of BiOCl, and holes in the VB of BiOCl likely transfer to the VB of Bi$_4$O$_5$I$_2$. Thus, it is a typical type II heterojunction (Fig. 6d).

In the contrary, when BiOCl and Bi$_4$O$_5$I$_2$ layers are in lateral contact (BOC-I-L heterojunction), the electrons of Bi$_4$O$_5$I$_2$ (30−3) facet would spontaneously transfer to BiOCl (001) facet through the carrier channels (Bi-O-Bi) until the balance of Fermi levels is reached, subsequently generating the strong interfacial electric field (IEF) at the interface of BOC-I-L heterojunction. The charge density difference of BOC-I-L

heterojunction (Fig. 6c) is computed to help understand charge transfer at the interface. The yellow color for BiOCl represents the electrons accumulation, and the cyan blue indicates the electrons depletion occurring on Bi$_4$O$_5$I$_2$. The charge density difference apparently shows the electrons transferred from Bi$_4$OI$_2$ to BiOCl at the BOC-I-L interface via the chemical bond (Bi-O-Bi) (Fig. 6c). The interfacial electrons accumulation and depletion would induce the energy bands of Bi$_4$O$_5$I$_2$ upwards and BiOCl bend downwards [37,39], respectively. Under the driving of IEF, the photogenerated electrons on the CB of BiOCl would easily transfer toward VB of Bi$_4$O$_5$I$_2$ and the photogenerated holes on the VB of Bi$_4$O$_5$I$_2$ would simultaneously transfer upward toward CB of BiOCl (Fig. 6d). This combination of electron-hole pairs at the interface of the BOC-I-L heterojunction indicates that the charge transfer pathway follows the Z-scheme [37–40].

3.3. Photogenerated charge separation efficiency and IEF

The IEF intensity is assessed to understand the relationship between the IEF and separation/transfer efficiency of photogenerated charges. The IEF magnitude can be calculated via the method by reported Kanata et al. as follows [41–43]:

$$F_s = (-2\ V_s\rho/\varepsilon\varepsilon_0)^{1/2}$$

where F_s is the IEF intensity, ρ is the surface charge density (Fig. 7a), V_s means the surface voltage obtained by surface photovoltage spectrum (Fig. 7b), ε is the low-frequency dielectric constant, and ε_0 is the permittivity of free space. As shown in Fig. 7c, the BOC-I-V and BOC-I-L heterojunction show the higher IEF than BiOCl and $Bi_4O_5I_2$, suggesting that the fabrication of heterojunction can improve IEF effectively. BOC-I-L heterojunction displayed a much higher IEF (9.41) compared with the BOC-I-V because of the stronger chemical bond (Bi-O-Bi) connection than VDW force. The giant IEF would greatly promote spatial separation and transfer of photogenerated electrons and holes, which is beneficial to photocatalytic efficiency.

The carrier separation efficiency was measured by a series of photoelectric and photoelectrochemical measurements. In order to eliminate the effect of light absorption on the separation of photogenerated carrier, the loading ratio of $Bi_4O_5I_2$ to BiOCl (001) and (110) facets were controlled to ensure similar light absorption performance. The UV–vis diffuse reflectance spectroscopy (DRS) shows that BOC-I-V and BOC-I-L heterojunctions with the same loading ration have approximately equivalent photo-absorption and the same absorption edges of 433 nm (Fig. S18). In addition, with the increase of loading amount of $Bi_4O_5I_2$,

the absorption edges of BOC-I-V and BOC-I-L heterojunctions appeared gradually red-shifted (Fig. S19).

The separation efficient of photogenerated electrons and holes in the BOC-I-V and BOC-I-L heterojunctions are compared by using transient photocurrent, electrochemical impedance spectroscopy (EIS), photoluminescence (PL) spectroscopy, and the surface photovoltage (SPV). The photocurrent intensity of BOC-I-L Z-scheme heterojunction is the highest, which is approximately twice that of BOC-I-V heterojunction, and five times that of pristine BiOCl, suggesting that BOC-I-L heterojunction is most favorable for electron transfer under the simulated sunlight (Fig. 7d). Quantitatively, the surface charge separation efficiency (η_{trans}) was calculated with adding the rapid electrons scavenger $MVCl_2$ in system [35]. The BOC-I-L has the largest η_{trans} (82.61%), followed by BOC-I-V (66.35%), $Bi_4O_5I_2$ (50.84%) and BiOCl (29.41%), respectively (Fig. S20). Besides, the EIS shows that the faster charge transfer kinetics in BOC-I-L heterojunction, because the arc radius of BOC-I-L is smallest among than that of BiOCl, $Bi_4O_5I_2$ and BOC-I-V heterojunction ($R_{BOC-I-L} < R_{BOC-I-V} < R_{Bi4O5I2} < R_{BiOCl}$) (Fig. 7e). The SPV further confirms that BOC-I-L heterojunction shows the fastest charge carrier transfer as indicated by the strong SPV signal around 325 nm (Fig. 7f). Meanwhile, photoluminescence (PL) spectra demonstrates that BOC-I-L Z-scheme heterojunction with the lowest emission
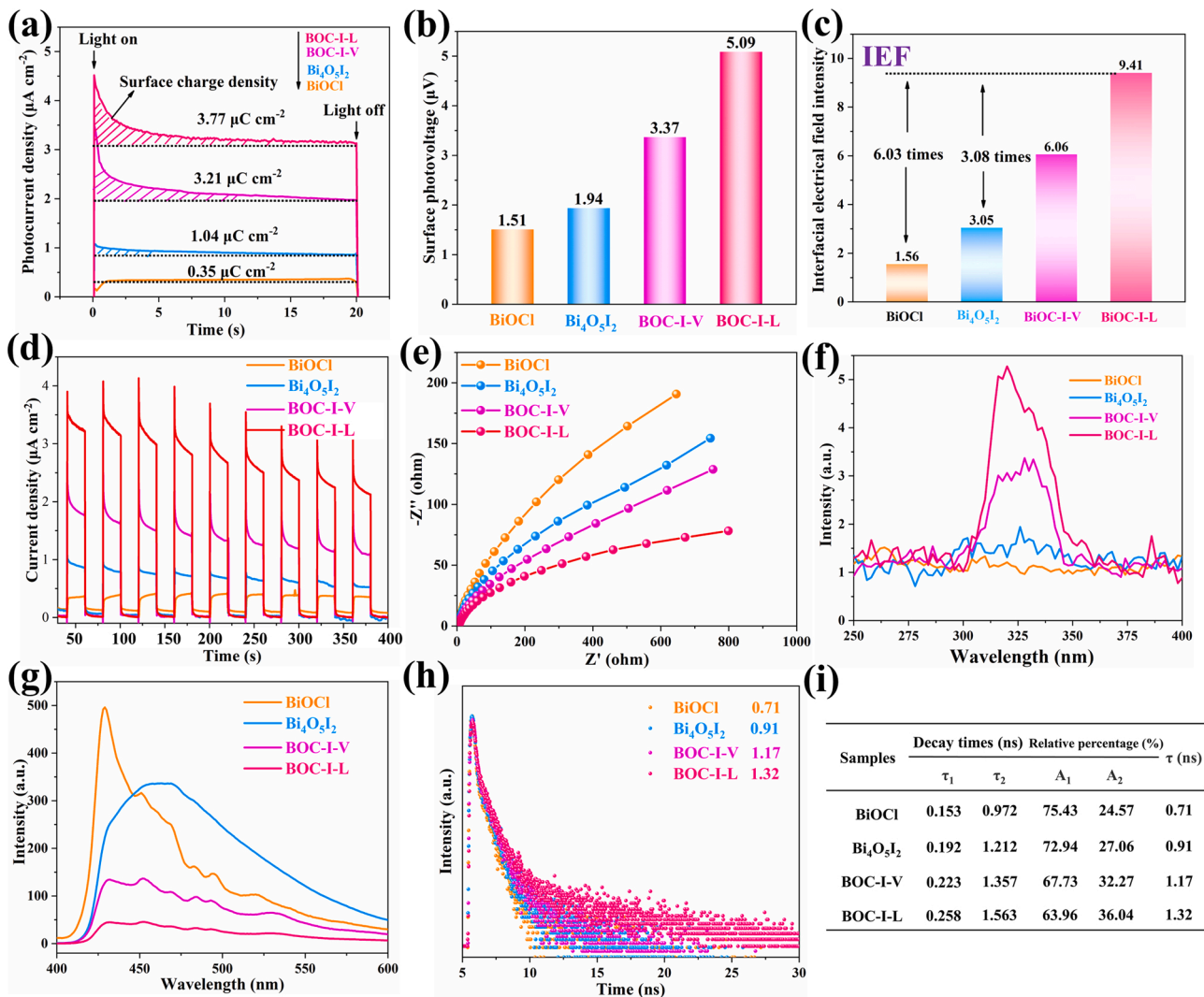
Fig. 7. (a) the surface charge density measured by transient photocurrent, (b) the surface voltage intensity, (c) the interfacial electric field intensity, (d) the transient photocurrent density and (e) equivalent circuit impedance (EIS) Nyquist plots, (f) Surface photovoltage spectra, (g) the steady-state photoluminescence (PL), (h) the time-resolved fluorescence emission decay spectra and (i) time-resolved fluorescence fitting results (table 1) of BiOCl, $Bi_4O_5I_2$, BOC-I-V heterojunction, BOC-I-L heterojunction.

peak intensity, suggesting the lowest recombination rate of photoexcited electrons and holes in BOC-I-L Z-scheme heterojunction (Fig. 7g). The time-resolved PL profile (Fig. 7h, i) also reveals that the longer lifetime of photogenerated charge carriers of BOC-I-L Z-scheme (τ = 1.32 ns) than that of BOC-I-V (τ = 1.17 ns), further suggesting that the recombination of carriers was inhibited due to the giant IEF, well lattice match and the directly carrier channel (Bi-O-Bi) at the BOC-I-L Z-scheme heterojunction interface.

3.4. Photocatalytic redox performances

The photocatalytic redox performances of all samples were evaluated by photocatalytic hydrogen production, Cr (VI) reduction and the degradation of phenol. After optimizing the mass ratio of BiOCl and $Bi_4O_5I_2$ (Fig. S21), BOC-I-L2 Z-scheme heterojunction exhibits the best photocatalytic H_2 evolution performance up to 1.91 $\mu mol \cdot h^{-1}$ with 50 mg photocatalyst (Fig. 8a), which is 8.68 times higher than that of pure BiOCl and 1.55 times higher than that of BOC-I-V under the simulated sunlight (Fig. 8b). Such a high performance also exceeds most of the reported BiOCl-based and Bi-based photocatalysts for H_2 production (Table S2, S3). In order to further explore the major factor affecting the photocatalytic hydrogen evolution process, a series of control experiments has been conducted. Light irradiation and photocatalysts are found to be necessary for the photocatalytic hydrogen production (Fig. S22).

The photo-reduced Cr (VI) performance of the samples are compared
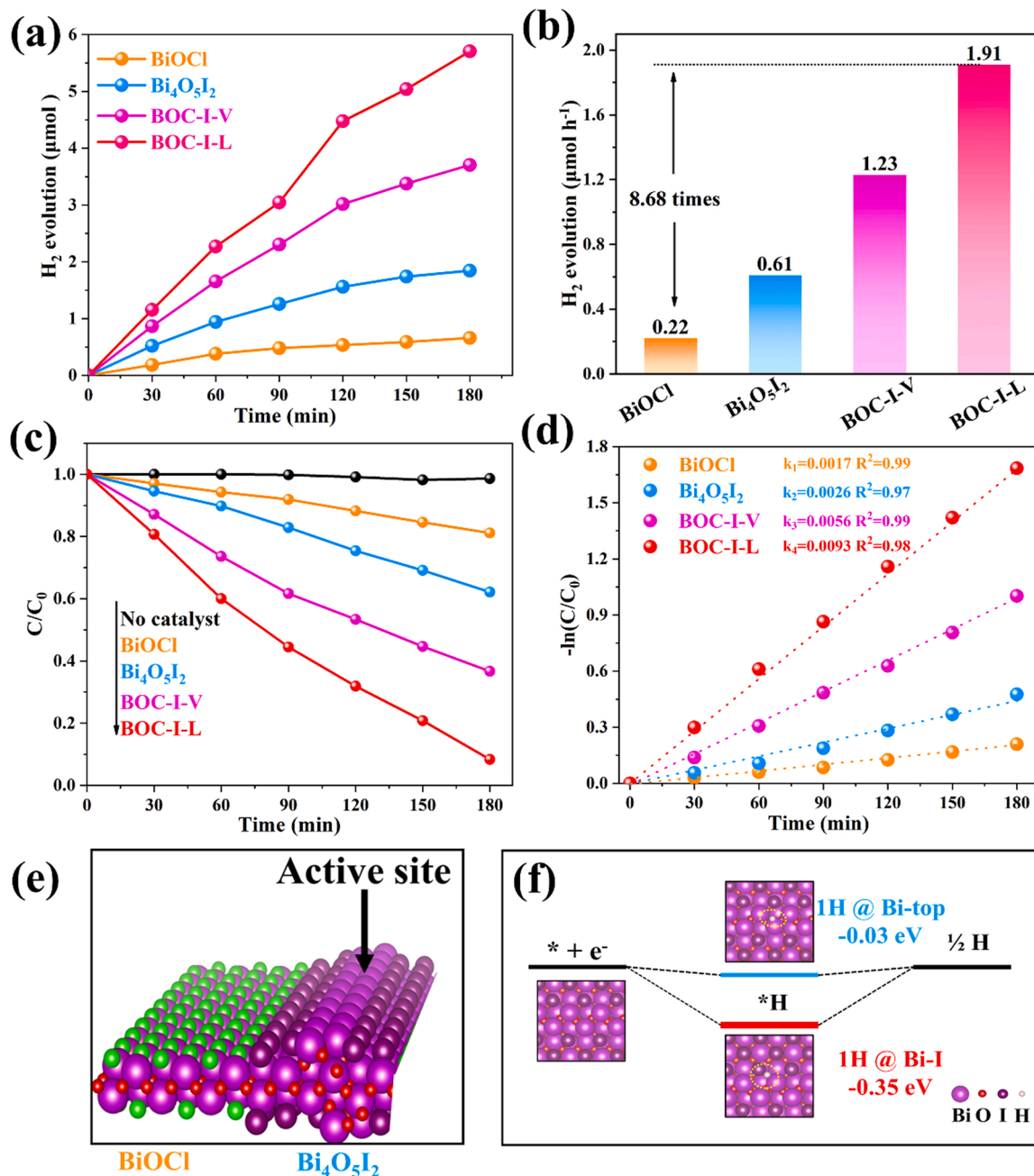
Fig. 8. (a) The photocatalytic H_2 evolution activity under the simulated sunlight, (b) the hydrogen evolution rate, (c) photocatalytic Cr (VI) reduction activity under the simulated sunlight and (d) pseudo-first-order kinetic constants of BiOCl, $Bi_4O_5I_2$, BOC-I-V and BOC-I-L heterojunctions, respectively, (e) schematic diagram of the active site on the BOC-I-L Z-scheme heterojunction, (f) Gibbs free energy diagrams of intermediates generated during H_2O to H_2 catalysis over BOC-I-L Z-scheme heterojunction.

and shown in Fig. 8c. The pure BiOCl and $Bi_4O_5I_2$ exhibit very low photoreduction activity on Cr (VI) with about 17% and 36% reduction within 180 min under the simulated sunlight irradiation. For the BOC-I-L Z-scheme heterojunction, above 90% Cr (VI) was reduced, far exceeding the BOC-I-V type II heterojunction (60%). The Cr (VI) photoreduction rate of BOC-I-L is 0.0093 min^{-1}, more than 1.56 times higher than that of BOC-I-V (0.0056 min^{-1}, Fig. 8d). The performance also exceeds that of most previously reported photocatalysts for Cr (VI) production (Table S4). In addition, the phenol photodegradation over the samples was carried out under the simulated sunlight (Fig. S23a), BOC-I-L Z-scheme heterojunction shows the most excellent phenol photodegradation performance in comparison with BOC-I-V, BiOCl and $Bi_4O_5I_2$, and the phenol degradation rate of BOC-I-L is 0.048 min^{-1}, nearly 2.1 times that of BOC-I-V (0.023 min^{-1}, Fig. S23). The performance of Bi-based photocatalysts for phenol removal is compared and listed in Table S5.

Fig. S23c-f display the degradation process of phenol over BOC-I-L, BOC-I-V, BiOCl and $Bi_4O_5I_2$. These results show that BOC-I-L Z-scheme heterojunction has the best photo-oxidation and photo-reduction performance. The stability of the BOC-I-L Z-scheme heterojunction is evaluated, the photocatalytic H_2 evolution of the BOC-I-L Z-scheme heterojunction under the simulated sunlight shows no significant decrease after four cycles (Fig. S24). The XRD, SEM and KPFM were performed to compare the sample before and after reaction. No noticeable change was observed, indicating good stability of the BOC-I-L Z-scheme heterojunction (Fig. S25-S27).

The surface-active sites are expected to reveal the capabilities of both capturing and releasing H atoms during the photocatalytic H_2 evolution [54,55]. The number of active sites can be estimated by the C-V test results. As shown in Fig. S28, the slope of as-prepared samples was acquired by fitting the C-V results qualitatively. The slope of BOC-I-L is 0.147, highest among all the samples studied, suggesting that the double layer capacitance is the largest at the interface between BOI-I-L Z-scheme heterojunction photocathode and electrolyte [44]. As a result, there are more active sites on the surface of BOC-I-L Z-scheme heterojunction to participate in reduction reaction, which benefits to the photocatalytic H_2 evolution [53]. To gain insight into the surface-active sites for photocatalytic H_2 evolution in the BOC-I-L Z-scheme heterojunction, we performed DFT calculation to evaluate the adsorption energy. As the most electrons are accumulated on CB of $Bi_4O_5I_2$, the active centers are mainly distributed on the $Bi_4O_5I_2$ (30−3) facet (Fig. 8e). In addition, the adsorption energies of Bi atoms in 1 H@Bi-top and 1 H@Bi-I were calculated and shown in Fig. Table S1. The adsorption energy of 1 H@Bi-top is − 0.03 eV, and the adsorption energy of 1 H@Bi-I is − 0.35 eV (Fig. 8d). The calculated results suggest that

1 H@Bi-I has the most appropriate adsorption energy, which facilitates H atom adsorption and release after reaction, and thereby photocatalytic H_2 evolution.

3.5. Photocatalytic mechanism of BOC-I-V and BOC-I-L heterojunctions

Based on the above analysis, possible photocatalytic mechanisms of BOC-I-V and BOC-I-L heterojunctions are proposed and shown in Fig. 9a and b, respectively. Upon light irradiation, photoexcited electron-hole pairs are generated in both BiOCl and $Bi_4O_5I_2$, which directionally migrate under the driving force of interfacial electrostatic field. For the BOC-I-V heterojunction (Fig. 9a), the photogenerated charge transfer fit well the type II model based on weak interfacial electric field, with photogenerated electrons from $Bi_4O_5I_2$ transferring to the BiOCl (001) facet that subsequently participate in photocatalytic hydrogen production and photoreduction of Cr (VI). Meanwhile, the photogenerated holes in BiOCl transfer to $Bi_4O_5I_2$, which could directly degrade phenol into CO_2 and H_2O. In addition, the photogenerated electrons could directly react with the surface absorbed O_2 to generate abundant $\cdot O_2^-$ and participate in phenol degradation. Subsequently, the active species for phenol degradation is h^+ and $\cdot O_2^-$, which is confirmed by the capture experiment (Fig. S29a). Compared with the BOC-I-V heterojunction, the BOC-I-L heterojunction based on direct chemical bonding has stronger IEF, and its photocarrier transfer pathway (Fig. 9b) attributed to the Z-scheme model. The photogenerated electrons in BiOCl could be rapidly transferred to $Bi_4O_5I_2$ and recombine with the photogenerated holes in $Bi_4O_5I_2$. As a result, electrons accumulated in the CB of $Bi_4O_5I_2$ could participate in photocatalytic hydrogen production or photoreduction of Cr (VI). At the same time, the photogenerated holes left on the VB of the BiOCl could degrade phenol. The $\cdot O_2^-$, generated from electrons accumulated on the $Bi_4O_5I_2$ surface reacting with surface absorbed O_2, can also result in phenol decomposition (Fig. S29b). Therefore, the BOC-I-L heterojunction shows much stronger photo reduction and oxidation ability than BOC-I-V heterojunction due to the stronger IEF and Z scheme charge transfer pathway.

4. Conclusion

BiOCl/$Bi_4O_5I_2$ VHs coupled by VDW force and BiOCl/$Bi_4O_5I_2$ LHs formed by chemical bonds (Bi-O-Bi) have been successfully synthesized by a two-step hydrothermal method. The charge migration mechanism of BOC-I-V heterojunction fits the typical type II model, while the BOC-I-L heterojunction follows the Z-scheme, Due to stronger interfacial electric field, higher photocharge separation/transfer efficiency and more direct carrier channels, the BOC-I-L Z-scheme heterojunction
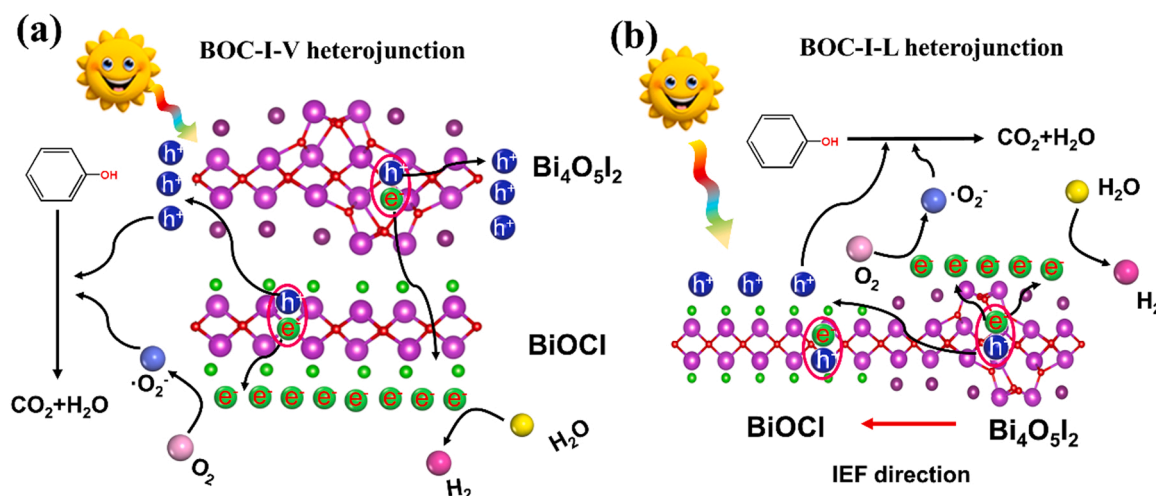

Fig. 9. Schematic illustration of photocatalysis mechanism diagram for BOC-I-V (a) and BOC-I-L (b) heterojunction.

showed the highest photo-reduction and photo-oxidation activities among all the samples studied. This study demonstrates the importance of combining facet engineering with heterojunction in the design of highly efficient photocatalysts.

CRediT authorship contribution statement

Daimei Chen conceived this project. **Daimei Chen, Hao Ding and Yi Zhong** designed the experiments. **Yi Zhong, Kang Xu** conducted the experiments. **Lianzhou Wang, Guocheng Lv, Weichang Hao and Yi Du** contributed to the characterizations and result analysis. **Yi Zhong, Chenglin Wu, Yanmei Feng, Daimei Chen and Jinzhong Zhang** wrote the manuscript.

Funding

Declaration of Competing Interest

The authors declare that they have no known competing financial interests or personal relationships that could have appeared to influence the work reported in this paper.

Data availability

Data will be made available on request.

Acknowledgments

Appendix A. Supporting information

Supplementary data associated with this article can be found in the online version at doi:10.1016/j.apcatb.2023.122554.

References

[1] L. Yu, X. Ba, M. Qiu, Y.F. Li, W. Shuai, W. Zhang, Z.F. Ren, Y. Yu, Visible-light driven CO_2 reduction coupled with water oxidation on Cl-doped Cu_2O nanorods, Nano Energy 60 (2019) 576–582.

[2] H. Xu, X.M. Liu, Hao Li, L.Z. Zhang, O_2 activation and $^1O_2$ generation over phosphate modified BiOCl for efficient photodegradation of organic pollutants, Appl. Catal. B Environ. (2022), 121520.

[3] Y. Li, A. Xu, Y. Lum, X. Wang, S. Hung, B. Chen, Z. Wang, Y. Xu, F. Li, J. Abed, J. Huang, A. Rasouli, J. Wicks, L. Sagar, T. Peng, A. Ip, D. Sinton, H. Jiang, C. Li, E. Sargent, Promoting CO_2 methanation via ligand-stabilized metal oxide clusters as hydrogen-donating motifs, Nat. Commun. 11 (2020) 6190.

[4] Y. Xia, Z. Tian, T. Heil, A. Meng, B. Cheng, S. Cao, M. Antonietti, Highly selective CO_2 capture and its direct photochemical conversion on ordered 2D/1D heterojunctions, Joule 3 (2019) 2792–2805.

[5] L. Mascaretti, A. Dutta, S. Kment, V.M. Shalaev, A. Boltasseva, R. Zboril, A. Naldoni, Plasmon-enhanced photoelectrochemical water splitting for efficient renewable energy storage, Adv. Mater. 31 (2019) 1805513.

[6] S. Huang, Y. Wang, J. Wan, Z. Yan, Y. Ma, G. Zhang, S. Wang, $Ti_3C_2T_X$ as electron-hole transfer mediators to enhance AgBr/BiOBr Z heterojunction photocatalytic for the degradation of Tetrabromobisphenol A: mechanism insight, Appl. Catal. B Environ. 319 (2022), 121913.

[7] Y. Lu, Y. Yang, X. Fan, Y. Li, D. Zhou, B. Cai, K. Zhang, Boosting charge transport in $BiVO_4$ photoanode for solar water oxidation, Adv. Mater. 34 (2022) 2108178.

[8] Y. Dou, L. Zhang, X. Xu, Z. Sun, T. Liao, S.X. Dou, Atomically thin non-layered nanomaterials for energy storage and conversion, Chem. Soc. Rev. 46 (2017) 7338.

[9] J. Di, X.X. Zhao, C. Lian, M.X. Ji, J.X. Xia, J. Xiong, W. Zhou, X.Z. Cao, Y.B. She, H. L. Liu, K.P. Loh, S.J. Pennycook, H.M. Li, Z. Liu, Atomically-thin Bi_2MoO_6 nanosheets with vacancy pairs for improved photocatalytic CO_2 reduction, Nano Energy 61 (2019) 54–59.

[10] X. Zhao, Y. Xia, H. Li, X. Wang, J. Wei, X. Jiao, D. Chen, Oxygen vacancy dependent photocatalytic CO_2 reduction activity in liquid-exfoliated atomically thin BiOCl nanosheets, Appl. Catal. B Environ. 297 (2021), 120426.

[11] P. Wang, C. Jia, Y. Huang, X. uan, Van der Waals heterostructures by design: from 1D and 2D to 3D, Matter 4 (2021) 552–581.

[12] J. Shao, F. Chen, W. Su, Y. Zeng, H.W. Lu, Multimodal nanoscopic study of atomic diffusion and related localized optoelectronic response of WS_2/MoS_2 lateral heterojunctions, ACS Appl. Mater. Inter. 13 (2021) 20361–20370.

[13] L. Wu, C. Cong, J. Shang, W. Yang, Y. Chen, J. Zhou, T. Yu, Raman scattering investigation of twisted WS_2/MoS_2 heterostructures: interlayer mechanical coupling versus charge transfer, Nano Res. 14 (2021) 2215–2223.

[14] C. Zhang, Y. Chen, J.K. Huang, X. Wu, L.J. Li, W. Yao, C.K. Shih, Visualizing band offsets and edge states in bilayer-monolayer transition metal dichalcogenides lateral heterojunction, Nat. Commun. 7 (2016) 1–6.

[15] J. Pu, H. Ou, T. Yamada, N. Wada, H. Naito, H. Ogura, T. Takenobu, Continuous color-tunable light-emitting devices based on compositionally graded monolayer transition metal dichalcogenide alloys, Adv. Mater. (2022) 2203250.

[16] K. Bogaert, S. Liu, J. Chesin, D. Titow, S. Gradecak, S. Garaj, Diffusion-mediated synthesis of MoS_2/WS_2 lateral heterostructures, Nano Lett. 16 (2016) 5129–5134.

[17] H. Yu, F. Chen, X. Li, H. Huang, Q. Zhang, S. Su, K. Wang, E. Mao, B. Mei, G. Mul, T. Ma, Y. Zhang, Synergy of ferroelectric polarization and oxygen vacancy to promote CO_2 photoreduction, Nat. Commun. 12 (2021) 4594.

[18] J. Li, L. Cai, J. Shang, Y. Yu, L. Zhang, Giant enhancement of internal electric field boosting bulk charge separation for photocatalysis, Adv. Mater. 28 (2016) 4059–4064.

[19] F. Chen, H. Huang, L. Guo, Y. Zhang, T. Ma, The role of polarization in photocatalysis, Angew. Chem. Int. Ed. 58 (2019) 10061–10073.

[20] H. Li, J. Li, Z. Ai, F. Jia, L.Z. Zhang, Oxygen vacancy-mediated photocatalysis of BiOCl: reactivity, selectivity, and perspectives, Angew. Chem. Int. Ed. 57 (2018) 122–138.

[21] H. Xu, X. Liu, H. Li, L. Zhang, O_2 activation and $^1O_2$ generation over phosphate modified BiOCl for efficient photodegradation of organic pollutants, Appl. Catal. B Environ. (2022) 121520.

[22] M. Ji, Y. Liu, J. Di, C. Rong, Z. Chen, J. Xia, N-CQDs accelerating surface charge transfer of $Bi_4O_5I_2$ hollow nanotubes with broad spectrum photocatalytic activity, Appl. Catal. B Environ. 237 (2018) 1033–1043.

[23] M. Zhao, J. Chen, B. Chen, X. Zhang, Z. Shi, Z. Liu, H. Zhang, Selective epitaxial growth of oriented hierarchical metal-organic framework heterostructures, J. Am. Chem. Soc. 142 (2020) 8953–8961.

[24] H.J. Lee, Y.J. Cho, W. Cho, Controlled isotropic or anisotropic nanoscale growth of coordination polymers: formation of hybrid coordination polymer particles, ACS Nano 7 (2013) 491–499.

[25] Y. Bai, T. Chen, P. Wang, L. Wang, L. Ye, Bismuth-rich $Bi_4O_5X_2$ (X= Br, and I) nanosheets with dominant {1 0 1} facets exposure for photocatalytic H_2 evolution, Chem. Eng. J. 304 (2016) 454–460.

[26] L. Hao, Q. Feng, Z. Yang, X. Cui, J. Wang, L. Zhang, New reaction pathway induced by plasmon for selective benzyl alcohol oxidation on BiOCl possessing oxygen vacancies, J. Am. Chem. Soc. 139 (2017) 3513.

[27] S. Wang, X. Cui, C.E. Jian, H. Cheng, M. Niu, J. Yu, W. Huang, Stacking-engineered heterostructures in transition metal dichalcogenides, Adv. Mater. 33 (2021) 2005735.

[28] M. Ji, J. Di, Y. Liu, R. Chen, K. Li, Z. Chen, H. Li, Confined active species and effective charge separation in $Bi_4O_5I_2$ ultrathin hollow nanotube with increased photocatalytic activity, Appl. Catal. B Environ. 268 (2020), 118403.

[29] H. Li, J. Shi, K. Zhao, L. Zhang, Sustainable molecular oxygen activation with oxygen vacancies on the {001} facets of BiOCl nanosheets under solar light, Nanoscale 6 (2014) 14168–14173.

[30] Y. Shi, J. Li, C. Mao, S. Liu, X. Wang, X. Liu, L. Zhang, Van Der Waals gap-rich BiOCl atomic layers realizing efficient, pure-water CO_2-to-CO photocatalysis, Nat. Commun. 12 (2021) 1–10.

[31] Y. Zhong, C. Wu, Y. Feng, D. Chen, Y. Wang, D. Hao, H. Ding, Enriched surface oxygen vacancies of BiOCl boosting efficient charge separation, whole visible-light absorption, and photo to thermal conversion, Appl. Surf. Sci. 585 (2022), 152656.

[32] R. Sinha, D. Friedrich, G. Zafeiropoulos, E. Zoethout, M. Parente, A. Bieberle-Hütter, Charge carrier dynamics and photocatalytic activity of {111} and {100} faceted Ag_3PO_4 particles, J. Chem. Phys. 152 (2020) 244710.

[33] J. Bian, Z. Zhang, J. Feng, M. Thangamuthu, F. Yang, L. Sun, L. Jing, Energy platform for directed charge transfer in the cascade Z-scheme heterojunction: CO_2 photoreduction without a cocatalyst, Angew. Chem. . Ed. 60 (2021) 20906–20914.

[34] C.H. Liu, Y.C. Chang, S. Lee, Y. Zhang, Y. Zhang, T.B. Norris, Z. Zhong, Ultrafast lateral photo-Dember effect in graphene induced by nonequilibrium hot carrier dynamics, Nano Lett. 15 (2015) 4234.

[35] M. Li, S. Yu, H. Huang, X. Li, Y. Feng, C. Wang, Y. Zhang, Unprecedented eighteen-faceted BiOCl with a ternary facet junction boosting cascade charge flow and photo-redox, Angew. Chem. Int. Ed. 58 (2019) 9517–9521.

[36] H. Liu, L. Huang, S. Ye, N. Yu, X. Tian, T. Du, Y. Zhang, Zhang, Intermediate-mediated strategy to horn-like hollow mesoporous ultrathin g-C_3N_4 tube with spatial anisotropic charge separation for superior photocatalytic H_2, Nano Energy 41 (2017) 738–748.

[37] F. Xu, K. Meng, B. Zhu, H. Liu, J. Xu, J. Yu, Graphdiyne: a new photocatalytic CO_2 reduction cocatalyst, Adv. Fun. Mater. 29 (2019) 1904256.

[38] C. Cheng, B. He, J. Fan, B. Cheng, S. Cao, J. Yu, An inorganic/organic s-scheme heterojunction H_2-production photocatalyst and its charge transfer mechanism, Adv. Mater. 33 (2021) 2100317.

[39] D. Zhao, Y. Wang, C.L. Dong, Y.C. Huang, J. Chen, F. Xue, L. Guo, Boron-doped nitrogen-deficient carbon nitride-based Z-scheme heterostructures for photocatalytic overall water splitting, Nat. Energy 6 (2021) 388–397.

[40] F. Liu, R. Shi, Z. Wang, Y. Weng, C.M. Che, Y. Chen, Direct Z-scheme hetero-phase junction of black/red phosphorus for photocatalytic water splitting, Angew. Chem. Int. Ed. 131 (2019) 11917–11921.

[41] K.-K. Takashi, M. Masayuki, T. Hideyuki, H. Yoshihiro, N. Taneo, Proc. SPIE Vol. 1286 (1990).

[42] G. Morello, F. Della Sala, L. Carbone, L. Manna, G. Maruccio, R. Cingolani, M. De, Giorgi, Intrinsic optical nonlinearity in colloidal seeded grown CdSe/CdS nanostructures: photoinduced screening of the internal electric field, Phys. Rev. B 78 (2008), 195313.

[43] J. Jing, J. Yang, W. Li, Z. Wu, Y. Zhu, Construction of interfacial electric field via dual-porphyrin heterostructure boosting photocatalytic hydrogen evolution, Adv. Mater. 34 (2022) 2106807.

[44] Y. Zhang, Y. Li, D. Ni, Z. Chen, X. Wang, Y. Bu, J.P. Ao, Improvement of $BiVO_4$ photoanode performance during water photo-oxidation using Rh-doped $SrTiO_3$ perovskite as a co-catalyst, Adv. Fun. Mater. 29 (2019) 1902101.

[45] J. Miao, Z. Xu, Q. Li, A. Bowman, S. Zhang, W. Hu, C. Wang, Vertically stacked and self-encapsulated van der Waals heterojunction diodes using two-dimensional layered semiconductors, ACS nano 11 (2017) 10472–10479.

[46] T. Yang, B. Zheng, Z. Wang, T. Xu, C. Pan, J. Zou, A. Pan, Van der Waals epitaxial growth and optoelectronics of large-scale WSe_2/SnS_2 vertical bilayer p-n junctions, Nat. Commun. 8 (2017) 1–9.

[47] S. Park, H. Wang, T. Schultz, D. Shin, R. Ovsyannikov, M. Zacharias, N. Koch, Temperature-dependent electronic ground-state charge transfer in van der waals heterostructures, Adv. Mater. 33 (2021) 2008677.

[48] H. Ben, Y. Liu, X. Liu, X. Liu, C. Ling, L. Liang, Zhang, Diffusion-Controlled Z-Scheme-Steered Charge Separation across PDI/BiOI Heterointerface for Ultraviolet, Visible, and Infrared Light-Driven Photocatalysis, Adv. Fun. Mater. 31 (2021) 2102315.

[49] A. Pant, Z. Mutlu, D. Wickramaratne, H. Cai, R.K. Lake, C. Ozkan, S. Tongay, Fundamentals of lateral and vertical heterojunctions of atomically thin materials, Nanoscale 8 (2016) 3870–3887.

[50] Y. Liu, J. Xu, M. Chen, Synthesis of direct Z-Scheme Bi_3NbO_7/BiOCl photocatalysts with enhanced activity for CIP degradation and Cr (VI) reduction under visible light irradiation, Sep. Purif. Technol. 276 (2021), 119255.

[51] X. Lin, A. Kumar, G. Sharma, M. Naushad, F.J. Stadler, A dual-functional integrated Ni_5P_4/g-C_3N_4 S-scheme heterojunction for high performance synchronous photocatalytic hydrogen evolution and multi-contaminant removal with a waste-to-energy conversion, J. Mol. Liq. 366 (2022), 120147.

[52] A. Kumar, G. Sharma, A. Kumari, C. Guo, M. Vo Naushad, F.J. Stadler, Construction of dual Z-scheme g-C_3N_4/$Bi_4Ti_3O_{12}$/$Bi_4O_5I_2$ heterojunction for visible and solar powered coupled photocatalytic antibiotic degradation and hydrogen production: Boosting via I^-/I^{3-} and Bi^{3+}/Bi^{5+} redox mediators, Appl. Catal. B Environ. 284 (2021), 119808.

[53] Y. Zheng, S. Chen, X. Yu, L. Ye, Nitrogen-doped carbon spheres with precisely constructed pyridinic-N active sites for efficient oxygen reduction, Appl. Surf. Sci. 598 (2022), 153786.

[54] X. Cao, Q. Luo, F. Song, G. Liu, S. Chen, Y. Lu, Effects of oxidative torrefaction on the physicochemical properties and pyrolysis products of hemicellulose in bamboo processing residues, Ind. Crop. Prod. 191 (2023), 115986.

[55] Y. Zheng, T. Gao, L. Ye, $CsPbBr_3$ quantum dots-decorated porous covalent triazine frameworks nanocomposites for enhanced solar-driven H_2O_2 production, Compos. Commun. 36 (2022), 101390.

[56] Y. Peng, N. Zhao, J. Liu, BiOCl Nanorings with Co-Exposed (110)/(001) Facets for Photocatalytic Degradation of Organic Dyes, ACS Appl. Nano Mater. 5 (2) (2022) 2476–2482.

[57] K. Zhao, L. Zhang, J. Wang, Q. Li, W. He, J.J. Yin, Surface structure-dependent molecular oxygen activation of BiOCl single-crystalline nanosheets, J. Am. Chem. Soc. 135 (42) (2013) 15750–15753.

[58] C. Zhou, S. Wang, Z. Zhao, Z. Shi, S. Yan, Z. Zou, A. Facet-Dependent, Schottky-junction electron shuttle in a $BiVO_4$ {010}-Au-Cu_2O Z-scheme photocatalyst for efficient charge separation, Adv. Fun. Mater. 28 (31) (2018) 1801214.

[59] H. Ben, Y. Liu, X. Liu, L. Zhang, Diffusion-controlled Z-scheme-steered charge separation across pdi/bioi heterointerface for ultraviolet, visible, and infrared light-driven photocatalysis, Adv. Fun. Mater. 31 (37) (2021) 2102315.

[60] X. Zhang, J. Zhou, D. Yang, S. Chen, J. Huang, Z. Li, $Cu_{2-x}S$ loaded diatom nanocomposites as novel photocatalysts for efficient photocatalytic degradation of organic pollutants, Catal. Today 335 (2019) 228.